Scientific Publications

International Journal of Mathematical, Engineering, Biological and Applied Computing, 2023, 2, 606
www.scipublications.org/journal/index.php/ijmebac
DOI: 10.31586/ijmebac.2023.606

Research Article

Pulsatile Blood Flow Simulation for Subject-Specific Geometry of a Human Aortic Arch

Zeba Shariff [1], M. Sivapragasam [2], Vinay M. D. Prabhu [3], R. Hariharan [4,*]

[1] Department of Electronics and Communication Engineering, M. S. Ramaiah University of Applied Sciences, Bangalore, India (Present address: Wipro GE Healthcare, Bangalore, India)

[2] Department of Aerospace Engineering, M. S. Ramaiah University of Applied Sciences, Bangalore, India

[3] Department of Radiology, M. S. Ramaiah Medical College and Hospitals, Bangalore, India

[4] Department of Electronics and Communication Engineering, M. S. Ramaiah University of Applied Sciences, Bangalore, India (Present address: Relecura Technologies, Bangalore, India)

*Correspondence: R. Hariharan (rharihar@ieee.org)

Abstract: Pulsatile blood flow in a subject-specific human aortic arch and its major branches is studied computationally for a peak Reynolds number of 1553 and a Womersley number of 22.74. The aortic geometry is constructed from the CT-scan images of a subject. The aorta has out-of-plane curvature and significant area variation along the flow direction. A physiologically representative pulsatile velocity waveform is applied as boundary condition at the inlet of the aorta. The primary velocity profiles are skewed towards the inner wall of the ascending aorta during the entire cardiac cycle. In the decelerating phase, reverse flow is noted along the inner wall and the magnitude of maximum velocity is about 50 % of the peak flow condition. Flow separation is observed in the inner wall of the ascending aorta during the decelerating and reverse flow phases of the cardiac cycle. In the accelerating phase, however, flow separation does not occur. The major observation of the present work is the existence of complex and asymmetrical vortical flow structures which are not observed either in simple curved pipes or in idealized aortic arch computational studies. The relative strength of the secondary flow with respect to the primary flow is quantified by means of Relative Secondary Kinetic Energy whose highest value is evaluated to be 1.202 occurring near the entrance of the right carotid artery during the maximum reverse flow condition. High values of wall shear stress is observed at distal of the left and right subclavian arteries, the bifurcation of brachiocephalic artery between right subclavian artery and right carotid artery, and proximal inner wall of descending aorta during the cardiac cycle. The wall shear stress at the bifurcations of the branches are low and oscillatory and generally correlates with the preferential sites for atherosclerosis. The flow structures on the aorta wall are explicitly highlighted by the limiting streamlines. The application of limiting streamlines to clearly elucidate the complex on-wall flow structures is one of the key contributions of the present study. During the decelerating and reverse flow phases several critical points are observed on the aortic wall. These complex flow structures vanish during the accelerating phase. The observations made in the present study will be helpful in creating accurate and clinically useful computational models.

Keywords: Aortic arch; Atherosclerosis; Biofluid Mechanics; Blood Flow Simulation; Computational Fluid Dynamics

How to cite this paper:
Shariff, Z., Sivapragasam, M., Prabhu, V. M. D., & Hariharan, R. (2023). Pulsatile Blood Flow Simulation for Subject-Specific Geometry of a Human Aortic Arch. *International Journal of Mathematical, Engineering, Biological and Applied Computing*, *2*(1), 1–19. Retrieved from https://www.scipublications.com/journal/index.php/ijmebac/article/view/606

Academic Editor:
Raja Marappan

Received: January 16, 2023
Accepted: March 29, 2023
Published: March 30, 2023

1. Introduction

Diseases related to the cardiovascular system are considered the most common cause of morbidity and mortality. It is estimated that about 17.9 million people died due to cardiovascular diseases in 2016. More than three-quarters of these deaths took place in

low- and middle-income countries [1]. In order to understand the pathogenesis of these diseases it becomes imperative to accurately describe and quantitatively assess the blood flow characteristics. Atherosclerosis is the deposition of lipids and fibrous elements in large arteries causing a decrease in vessel wall diameter and changes in the blood flow dynamics [2]. The localization data of atherosclerosis indicate that early atherosclerotic lesions tend to develop in the vicinity of arterial branching and curvature where blood flow patterns are quite complex [3]. It is also postulated that a correlation exists between certain fluid dynamical conditions and the biological response of the endothelial cells. The precise role of fluid dynamics on the localization of atherosclerosis is still a subject matter of study and debate. It is, however, widely believed that the shear stresses acting on the arterial wall are responsible for the mechanotransduction of the endothelial cells [4].

The aortic arch with its major branches is a particular region where the blood flow dynamics is complex due to curvature and torsion of the arch leading to skewed velocity profiles and secondary flows. Several past studies on flow in simple curved pipes relevant to aortic arch and encompassing a wide range of flow parameters have provided valuable physical insight. A simplified aortic geometry constructed from CAT scan images was used in Shahcheraghi et al. [5]. It was found that the primary velocity profiles were skewed towards the inner wall in the ascending aorta, and towards the outer wall in the descending aorta. Further, high wall shear stress was noted along the aorta outer wall in the vicinity of the branches. The study of Morris et al. [6] also utilized aorta geometry from CT scan images and simplified models were used for the computations. The axial velocity profile was found to be skewed towards the inner wall, and the shear stress was found to be similar in the models. The study of Benim et al. [7] employed an idealized geometric model of the aortic arch to study the physiological and extracorporeal circulation conditions and significant differences in the flow patterns and wall shear stress were found. Xuan et al. [8] performed a fluid-structure interaction study of a simplified geometric model of the aortic arch and found that the wall shear stress was high in the inner wall of the middle portion of the aortic arch. Wang et al. [9] performed a fluid-structure interaction study of an aorta modeled as a 180° curved pipe with only one branch. They found that the maximum values of von Mises stress occurs at the pipe inlet and the branch junction. The work of Krishna et al. [10], Zhu et al. [11], and Najjari et al. [12] consider only the simple 180° curved pipe without the branches. These studies lack subject-specific information which the medical practitioners are often interested in. In order to gain an understanding of the physiological parameters leading to these flow features subject-specific geometries of the aortic arch have to be considered.

Only recently subject-specific aortic geometries are being considered for analysis. Endo et al. [13] performed flow visualization studies in human aorta prepared from cadaver castings. They maintained steady-flow conditions corresponding to mid-systole in the experiments. It was observed that atherosclerotic lesions were found in proximal of the branches. Numata et al. [14] performed simulations for six different patient-specific aortic geometries constructed from CT images of the subjects. High oscillatory shear index was noted at the tip of the aneurysm in the subjects with arch aneurysm. Further, in subjects with dilated thoracic aorta, a helical flow pattern was observed. Soudah et al. [15] performed measurements, using 4D flow cardiovascular magnetic resonance, and simulations on an aortic geometry. It was shown that combination of both the techniques resulted in accurate estimation of the wall shear stresses. Belaghit et al. [16] performed computations on a realistic healthy aortic arch and that with a stent. They found that the stent limits the dilatation of the descending aorta. Bhuyan et al. [17] performed simulations for a cannulated aorta and found that the cannula must be placed at right angles to the aortic wall to minimize the sand blasting effect. It is thus seen that recent studies account for realistic aortic geometries and lead to subject-specific flow features.

The secondary flow induced by flow through curved pipes has been studied extensively due to its physiological and engineering applications. The secondary flows,

i.e., flows in planes perpendicular to the axis of the curved pipe, are caused due to the interaction between radial pressure gradient and centrifugal force and results in a pair of counter-rotating Dean vortices. The secondary flow structures are altered by the unsteadiness of the inflow leading to rich and complex flow topologies. A number of studies have investigated these structures due to oscillatory (zero-mean), pulsatile (non-zero-mean), and single-pulse inlet flow conditions. Physiological arterial flows are necessarily pulsatile. Furthermore, the presence of the aortic branches has a profound influence on the secondary flow structures. Many studies in the past have neither considered the branches or had the branches curtailed. In summary, the aortic arch with out-of-plane curvature and branches emanating from different planes in combination with pulsatile inflow conditions presents us a complicated flow problem.

In the light of the above discussion in the present study a subject-specific geometry of the aortic arch and its major branches is generated from the CT-scan data acquired from the institutional repository of M. S. Ramaiah Medical College and Hospitals, Bangalore, India. A careful computational study is performed using this geometry. This study has been cleared by the University Ethics Committee for Human Trials of the M. S. Ramaiah University of Applied Sciences, Bangalore, India. The present paper is arranged as follows. The pulsatile flow in a subject-specific human aortic arch is considered in the following section. Results are presented and discussed next. Finally, conclusions are given.

2. Materials and Methods

In this section the pulsatile blood flow simulation in a human aortic arch is considered. A reliable subject-specific blood flow simulation requires in decreasing order of modeling complexity and sensitivity, the arterial geometry, boundary conditions at the inlet and outlet, mechanical properties of the arterial wall and physical properties of blood. These issues are discussed in the following sections.

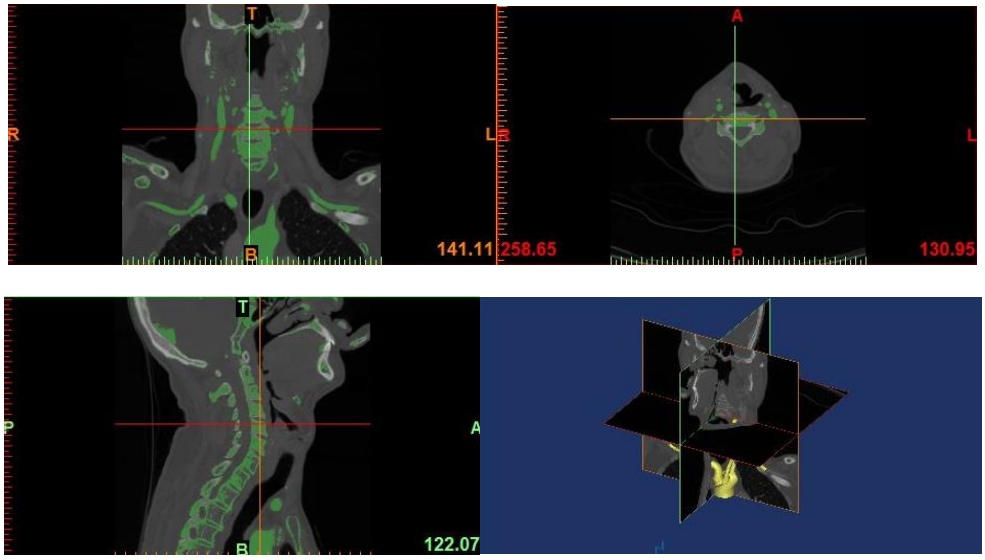

Figure 1. CT-scan images of the subject. The aorta can be seen in the bottom middle of the lower right frame colored in yellow.

2.1. Geometry modeling

The geometry for the present study is generated from the CT-scan images obtained from the institutional repository of M. S. Ramaiah Medical College and Hospitals, Bangalore, India. The scan data set is of a 66-year old male subject. The CT-scan data set

of the subject consists of 559 slices of the upper neck and chest in the form of Digital Imaging and Communications in Medicine (DICOM) images. These slices are stitched together to reconstruct the three-dimensional geometry of the aortic arch and the major branches. The aorta can be seen in the bottom middle of the lower right frame in Figure 1. The descending portion of the aorta is not part of the CT-scan data set. This fact necessitated the construction of the descending aorta. It is constructed using an exponential form given by the following equation:

$$D(s) = k_1 + k_2\, e^{-k_3 s} \tag{1}$$

where D is the diameter of the aorta and s is the arc length along the aorta. The values of k_1, k_2 and k_3 are obtained as follows. Firstly, the diameter variation along the arc length of the aortic arch is obtained from the three-dimensional geometric model and plotted. Then an exponential curve fit is done to this data set to obtain k_2 and k_3. This function is then shifted by an amount k_1 so that the aortic arch and the descending aorta merge smoothly without any geometric discontinuity. k_1, k_2 and k_3 are obtained to be 1.5, 30.482 and 0.004, respectively, as a best fit to the present geometry. The motivation for employing an exponential function is based on the observation that the aorta exhibits significant taper with the cross-sectional area reducing by about fifty percent [18]. The particular exponential form in eq. (1) is suggested by Li [19] based on in vivo measurements. It must be mentioned that only the descending portion of the aortic arch is modeled as an exponential function while the rest of the aortic arch including the branches are faithfully reconstructed from the actual scan data for the chosen subject.

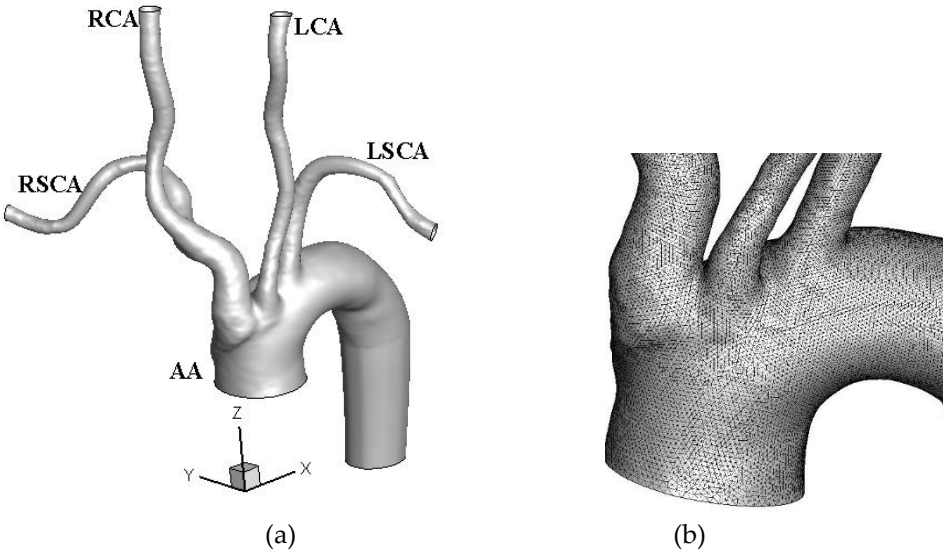

Figure 2. (a) Geometry of aortic arch and its major branches used in the present study and (b) computational grid.

In the present study, the right subclavian artery (RSCA), right carotid artery (RCA), left carotid artery (LCA) and left subclavian artery (LSCA) are also included along with the aortic arch (AA). In many studies in the past these branches had not been considered or had been curtailed. However, in the present study these branches are retained due to the interest in studying the fluid dynamics in these branches too. The aorta exhibits significant out-of-plane curvature for the present subject. Further, the branches also show out-of-plane curvature and are oriented along different axes. It may be noted that such variations are subject-specific and are difficult to account for in studies which use

simplified geometric models. It must be mentioned here that the geometry preparation process takes up a substantial proportion of the overall time and effort. Conventionally, the CT-scan imaging, recreating the three-dimensional aortic geometry, generating computational grid, performing computations and post-processing have been done as individual activities. At present, the entire CT-to-CAD-to-CFD workflow can be seamlessly integrated and automated. For example, Taylor et al. [20] and Driessen et al. [21] reported such results using a software, HeartFlow CT-Flow. Further, it is reported in [22] that this process takes a few hours. Coenen et al. [23] reported computational times ranging from 30 minutes to 2 hours using Siemens Healthcare software. Jiang et al. [24] mentioned 35 minutes for the computations using AccuFFRct. It must, however, be noted that these studies estimate only the fractional flow reserve (FFR) which is the ratio of the distal and proximal pressures across a stenotic lesion. In order to obtain detailed flow characteristics, computations of the kind advocated in the present study are to be performed. The present compute-intensive simulations took 42 hours on a desktop computer workstation with 16 GB RAM, Intel i5 processor (3.10 GHz). The simulation time can be drastically reduced by employing workstations with better memory and parallel processing capabilities. The final three-dimensional geometry of the aortic arch and its major branches is shown in Figure 2(a). The computational grid for the aorta geometry is generated in the meshing software. An unstructured grid is generated using tetrahedral meshing scheme. Grid smoothening operation is carried out to smoothen the grid globally. The total number of cells in the computational domain is 8.42×10^5. Care is taken in maintaining grid uniformity as can be seen in Figure 2(b).

2.2. Computational modeling

The incompressible, unsteady Navier-Stokes equations

$$\nabla \cdot u = 0 \ , \qquad \frac{\partial u}{\partial t} + u \cdot \nabla u = -\frac{1}{\rho}\nabla p + \nu \nabla^2 u \tag{2}$$

are solved numerically using the CFD code Fluent. Here $\boldsymbol{u}$ is the velocity vector, ρ is the uniform fluid density, p is the pressure and v is the fluid kinematic viscosity. The convective terms in the Navier-Stokes equations are discretized by a second-order upwind scheme and the viscous terms by a second-order central differencing scheme. The SIMPLE algorithm is employed for pressure-velocity coupling. The unsteady numerical formulation is second-order implicit. For the pulsatile computations one time-period is divided into 500 time steps for time-accurate calculations. In previous numerical experiments with the unsteady simulations in a subject-specific human carotid artery bifurcation it was shown that the unsteady results are independent of the time-step when one time-period was divided into 500 time steps for time-accurate calculations [25]. The convergence of the residuals is 10^{-6}. All calculations are done in double-precision arithmetic.

The computational procedure is first verified by performing a systematic grid independence study with coarse, medium and fine grids for a curved pipe geometry with radius ratio, a/R = 1/7 (shown in the inset of Figure 3) and Reynolds number 242. This study is performed with 1.08×10^5 (coarse grid, named G1), 2.19×10^5 (medium, G2) and 4.04×10^5 (fine, G3) cells. The axial velocity profile, non-dimensionalized by the inlet velocity, at $\theta = 160^\circ$ for the results from the three grids is plotted in Figure 3. It is observed that the results are convincingly grid independent. Further, to formally quantify the discretization error the Grid Convergence Index (*GCI*) [26] is evaluated by choosing the axial velocity at $\theta = 160^\circ$, $x/a = 0.75$ as the variable η. This x/a location is chosen since a

slightly larger difference is seen in the velocity profiles thus making the *GCI* test more stringent. The results are summarized in Table 1. Since the medium grid has a comparatively low value of discretization error it is chosen for computations. The grid for the aortic geometry is generated using the same meshing strategy and mesh distribution as the medium grid.

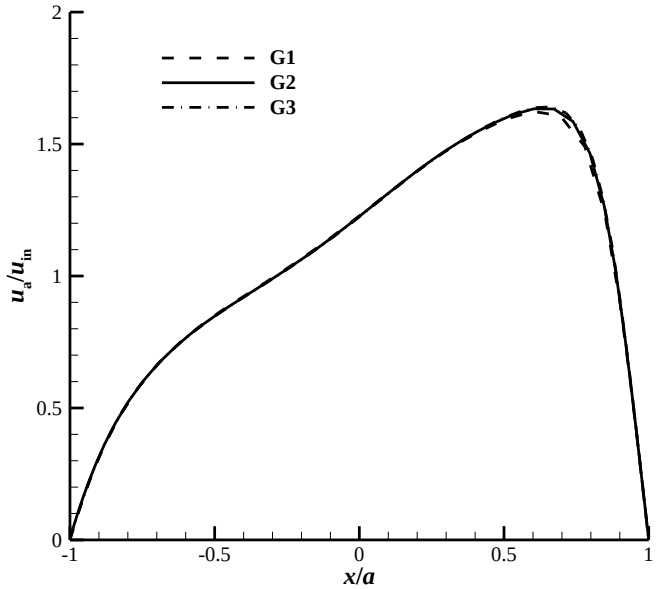

Figure 3. Comparison of axial velocity profile at $\theta = 160^{\circ}$ for the three grids. The axial velocity is non-dimensionalized by the inlet velocity.

Table 1. Summary of grid independence study.

Grid	No. of cells	η	*GCI* %
G1	1.08×10^5	1.53065	
G2	2.19×10^5	1.56148	1.67
G3	4.04×10^5	1.57288	0.76

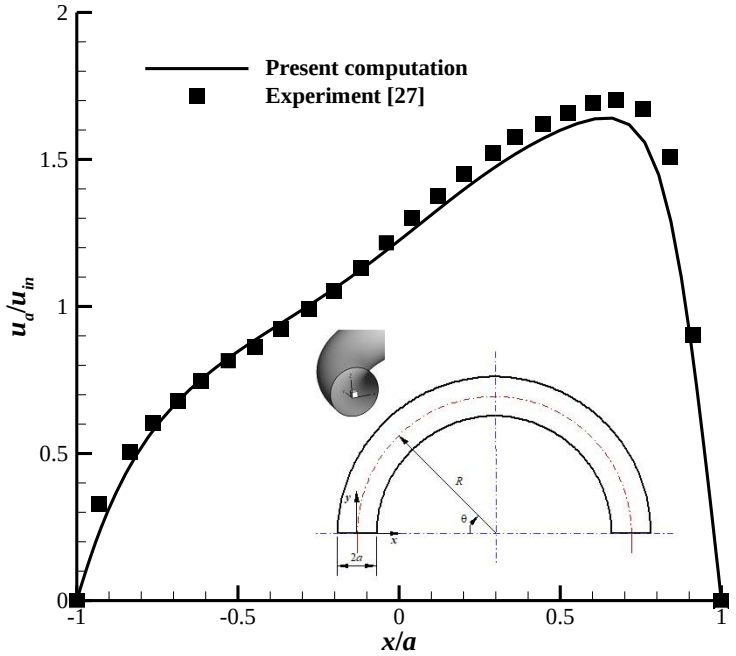

Figure 4. Comparison of axial velocity profile at θ = 160° from present computations and experiments.

The axial velocity profile at an azimuthal location θ = 160° is compared with the experimental results of [27] in Figure 4. A good agreement is obtained indicating a validation of the present computational procedure.

For the aortic arch simulations, the working fluid is taken to be blood with density ρ = 1060 kg/m^3 and dynamic viscosity μ = 0.00309 kg/m-s. It is assumed that blood behaves as a Newtonian fluid with a constant viscosity coefficient since shear rates in large arteries are usually relatively large validating this assumption. It is further assumed that the walls of the arteries are rigid. These two assumptions are not very restrictive and also making them subject-specific is not easy. Typical variations of arterial diameter are only about ± 2 % during the pulsatile cycle.

At the inlet of the aorta a pulsatile velocity waveform adapted from [5] is applied as inlet boundary condition. The application of this boundary condition chosen from the literature is necessiated because the CT-scan data set used in the present study is retrospectively obtained from the institutional repository after a thorough search covering a large number of subjects. The velocity waveform boundary condition applied at the inlet of the aortic arch is physiologically representative and has been successfully used in other simulations as well. The inlet velocity waveform employed in the present study is shown in Figure 5, where u_{max} is the peak inlet velocity. This waveform comprises of decelerating, reversed, zero and accelerating flow segments. In the present computations the inlet velocity waveform is represented by a Fourier series as follows:

$$u(t) = a_0 + \sum_{n=1}^{\infty} \left(a_n \cos nt + b_n \sin nt \right) \tag{3}$$

where a_n and b_n are the Fourier coefficients. In Eq. (3), the dimensional values of u and t are used to obtain a_n and b_n using the curve fit toolbox in MATLAB. It is found sufficient to accurately represent the inlet velocity waveform using the first eight harmonics. Equation (3) is programmed by means of a user-defined function in the flow solver and applied as boundary condition at the inlet of the aorta. Further, the velocity profile at the aorta inlet is uniform. Blood leaving the aortic valve and entering the aorta is known to exhibit a relatively flat velocity profile.

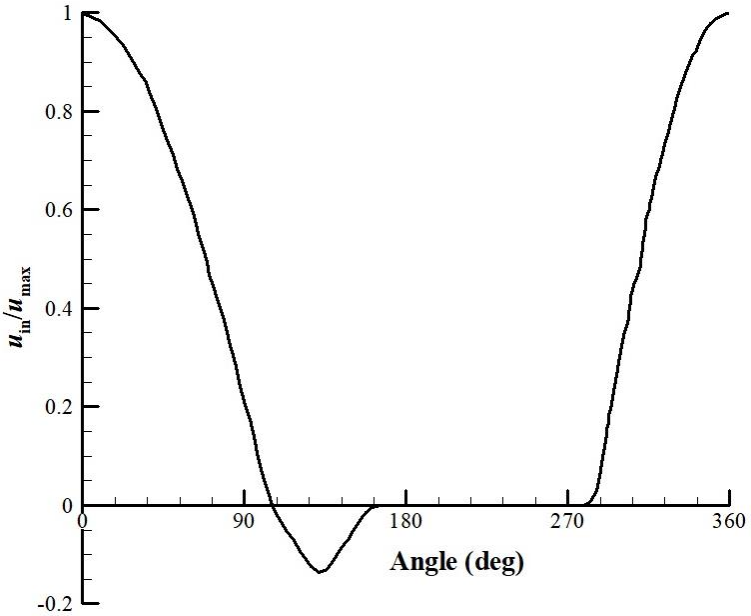

Figure 5. Inlet velocity waveform.

The flow conditions that prevail at the outlet of the aorta and the branches are far less clear from the literature. Some studies have applied a specified flow distribution among the aorta and the branches, while others have applied pressure boundary conditions. In the absence of consistent information zero-pressure outlet boundary condition is applied at the outlet of the aorta and the four branches in the present study. Regardless of the specific choice of the boundary condition it is important to ensure, and is done in the present study, that global mass conservation is satisfied. The no-slip boundary condition is applied on all the arterial walls.

Computations are performed for a peak Reynolds number of 1553. This Reynolds number is based on the maximum velocity and diameter at the aorta inlet. The maximum velocity is evaluated based on a cardiac output of 6.4 litres per minute which corresponded to rest condition of a normal individual [28]. The pulse rate is 64 beats per minute which results in a Womersley number of 22.74. The Womersley number is an important dimensionless parameter to characterize the pulsatile nature of flow. It is defined as

$$W = \frac{D}{2}\sqrt{\frac{\omega}{\nu}} \tag{4}$$

where ω is the heart rate in radians/sec. It is the ratio of the unsteady inertial to viscous forces and has a physical significance similar to Reynolds number for steady flows. For large values of W, inertial forces dominate the viscous forces and consequently the velocity profiles are more flat in the core of the artery. For the pulsatile simulations, a steady-state solution is first obtained with Re = 1553 and this solution is used as an initial condition for the unsteady computations. The flow achieved periodicity in two cycles and the results of the third cycle are presented in the following sections.

3. Results and Discussion

Before a detailed analysis of the results is presented, it is prudent to introduce and also clarify the need for defining primary and secondary velocity components in the aortic geometry. The component of velocity normal to any cross-sectional plane of interest is the primary velocity, $\boldsymbol{u}_p$, and that component of velocity along the cross-sectional plane is the

secondary velocity, $\boldsymbol{u}_s$. The computations are performed in the flow solver by fixing a global x-y-z Cartesian coordinate system and the cross-sectional planes in the aortic geometry are generally not aligned with any of these axes. Thus, evaluating the primary and secondary velocity components from the native solution of the flow solver is a non-trivial task. To evaluate $\boldsymbol{u}_p$ and $\boldsymbol{u}_s$, the procedure of [29] is followed. Briefly, the procedure involves taking the inner product of the velocity vector $\boldsymbol{u}$ and the unit normal vector pointing along the primary flow direction $\boldsymbol{n}$ and then constructing the primary velocity vector $\boldsymbol{u}_p$. The secondary velocity vector $\boldsymbol{u}_s$ is obtained by vectorial subtraction of the velocity and the primary velocity vectors.

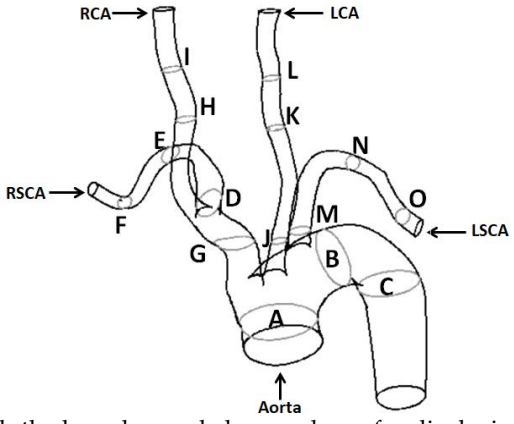

Figure 6. Aortic arch with the branches and chosen planes for displaying primary and secondary velocity components.

The contours and vectors of primary and secondary velocities are displayed at several select planes in the aortic arch and the branches. These planes are shown in Figure 6. The velocity components are plotted at select phase angles in the pulsatile cycle on those planes. The chosen phase angles are $\phi = 0^\circ$, 75°, 130° and 320° representing maximum flow, decelerating flow, maximum reverse flow and accelerating flow, respectively, of the cardiac cycle; see Figure 5. Furthermore, the velocity components are non-dimensionalized by the maximum inlet velocity.

3.1. Primary velocity distribution

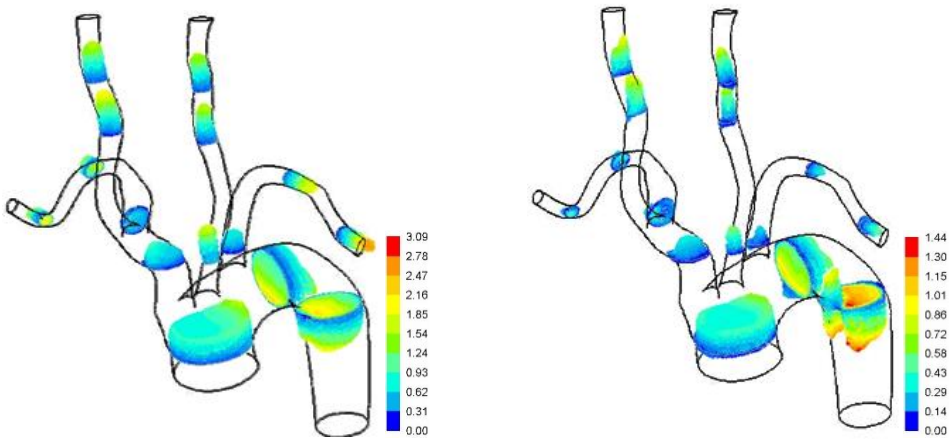

(a) (b)

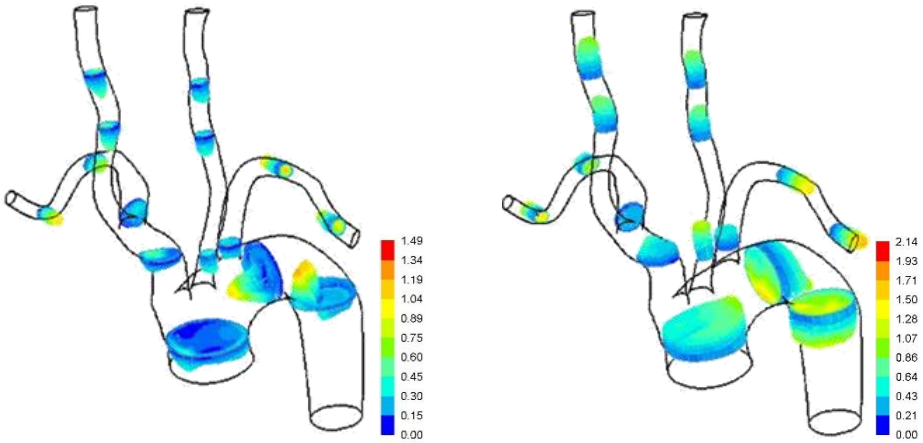

(c) (d)

Figure 7. Primary velocity vectors at (a) $\phi = 0^{\circ}$ (b) $\phi = 75^{\circ}$ (c) $\phi = 130^{\circ}$ and (d) $\phi = 320^{\circ}$.

The primary velocity vectors are shown in Figure 7. In Figures 7 to 9 the contour levels are scaled between minimum and maximum values at that ϕ for the sake of clarity in presentation. At $\phi = 0^{\circ}$, the velocity profile is skewed towards the inner wall in plane A in ascending aorta and in plane B in the mid-arch of aorta slightly away from the LCA. The velocity profile is skewed to a lesser extent at the inner wall at plane C in descending aorta. The velocity magnitude at both the right and left subclavian arteries is high at the mid region and less skewed at the walls in planes D, E, F, M, N and high in plane O. At the right and left carotid arteries the magnitude of velocity is reduced at the proximal of the branches of planes G, J and high at the distal wall in planes H, I, K and L.

In the decelerating phase at $\phi = 75^{\circ}$, there is reverse flow in the inner wall at plane B which is more pronounced at plane C. Mild reverse flow pattern is also seen at planes H, I, K and L. It is also noted that the magnitude of maximum velocity is nearly half of that during the peak flow condition. The $\phi = 130^{\circ}$ flow condition is different from other phases of the cardiac cycle because of the tendency of the blood to go back to the root of aorta where the aortic valve prevents the blood flowing to the left ventricle. Even at this ϕ flow reversal is observed at inner wall of planes B and C and to a lesser extent at plane A. During the accelerating phase of the cycle at $\phi = 320^{\circ}$, the velocity vectors are qualitatively similar to that observed during $\phi = 0^{\circ}$. The flow reversal noted during the decelerating and reverse flow phases is not seen now.

3.2. Secondary velocity distribution

The secondary flow field in the aortic geometry is expected to be complicated than that in a simple curved pipe due to out-of-plane curvature of the aortic arch and also due to the presence of the branches. The spatio-temporal evolution of the secondary flow field is traced only in the aortic arch for the sake of brevity. The contours of secondary flow velocity magnitude superimposed with secondary flow vectors are plotted in Figure 8. The contours are plotted from the posterior side with the primary velocity pointing into the sheet of paper. As the view is along the flow in each of these figures the right hand side is the inner wall and the left hand side is the outer wall.

At $\phi = 0^{\circ}$, in plane A the secondary flow is towards the inner wall. In plane B three vortices are present, one near the 5 o'clock position with a clockwise (CW) sense of rotation and another vortex near the 10 o'clock position with a counter clockwise (CCW) sense of rotation. These vortices are close to the secondary boundary layer. A third vortex is seen in the inviscid core flow with CW rotation. There is also sign of an incipient fourth

vortex at 3 o'clock position. In plane C, a pair of vortices are seen near the secondary boundary layer at 2 o'clock and 7 o'clock positions. At $\phi = 75^{\circ}$, in plane A, the secondary flow is similar to that seen at $\phi = 0^{\circ}$. In plane B, the three vortices seen at $\phi = 0^{\circ}$ persist. In addition the fourth vortex at 3 o'clock position becomes distinct. In plane C, the two vortices seen at $\phi = 0^{\circ}$ persist with the same sense of rotation, and in addition a third vortex is seen at about 5 o'clock position with a CCW rotation.

At $\phi = 130^{\circ}$, in plane A, the secondary flow is from the inner and outer walls towards the dorsal of the plane A. There are two vortices close to the boundary layer of the outer wall at 7 o'clock and 10 o'clock positions with CW and CCW sense of rotation, respectively. In plane B, the four vortices observed at $\phi = 75^{\circ}$ persist. In plane C, two vortices are present at 2 o'clock and at 6 o'clock positions in the core having CW and CCW sense of rotation, respectively. At $\phi = 320^{\circ}$, in plane A, the secondary flow is towards the top inner wall. In plane B, there is a bulk CW secondary flow motion with a central vortex. In plane C, the secondary flow is from dorsal to ventral side of this plane. Interestingly, the otherwise complex secondary flow structures noted in the previous ϕ are not seen during this phase due to the stabilizing nature of the accelerating flow. It may be remarked here that the complex and asymmetrical secondary flow patterns in the aorta shown in Figure 8 are not seen in simple curved pipe. Previous studies that have considered either simple curved pipes or idealized models of the aortic arch exhibit the classical symmetrical Dean-type, or deformed Dean-type, or Lyne-type vortices. However, geometric features of the aorta that are subject-specific like out-of-plane curvature of the arch and the presence of the major branches emanating from different planes in addition to the pulsatility of the flow leads to the formation of complicated flow structures. It is, therefore, necessary to perform subject-specific simulations to account for these intricate flow features.

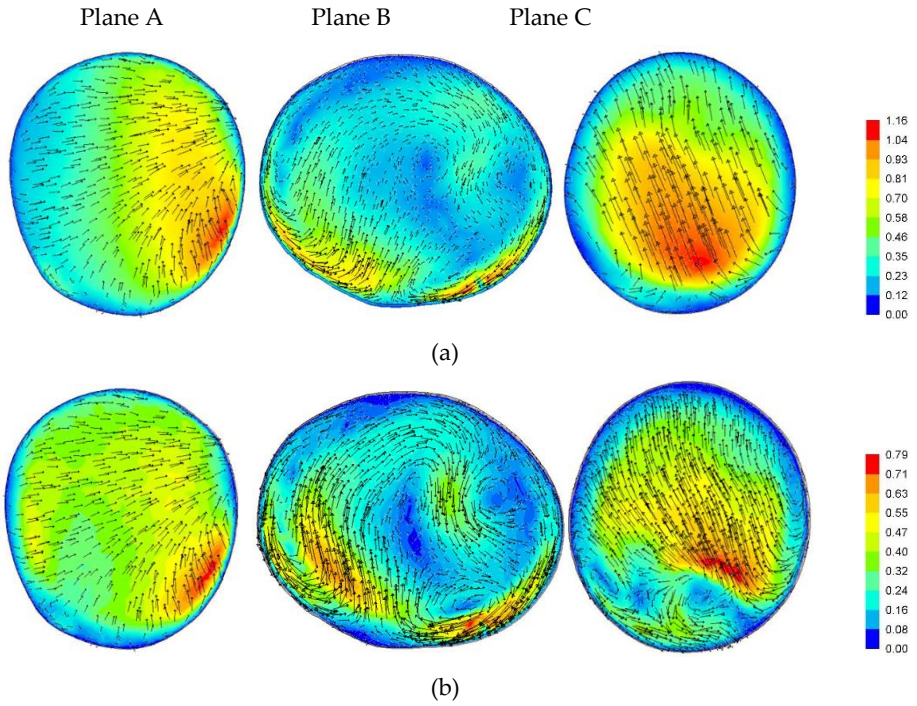

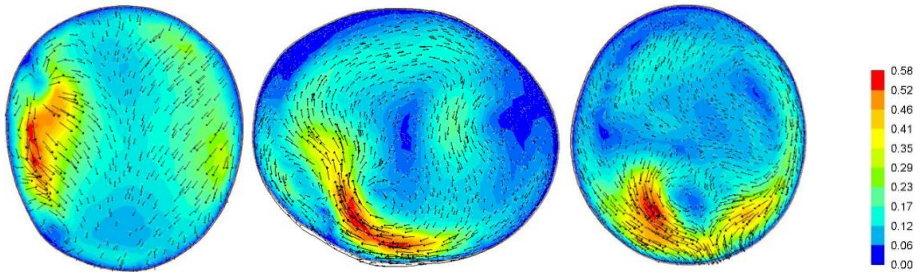

(c)

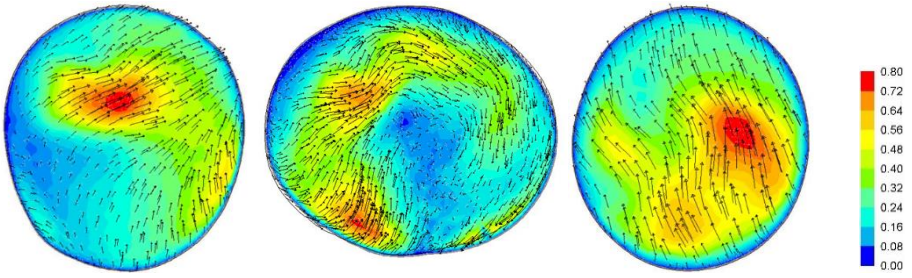

(d)

Figure 8. Contours of secondary velocity magnitude superimposed with secondary velocity vectors at (a) $\phi = 0^{\circ}$ (b) $\phi = 75^{\circ}$ (c) $\phi = 130^{\circ}$ and (d) $\phi = 320^{\circ}$.

To quantify the relative strength of the secondary flow with respect to the primary flow a quantity termed the Relative Secondary Kinetic Energy (RSKE) is employed which is defined as follows [29]:

$$RSKE = \sqrt{\frac{\int |\boldsymbol{u}_s|^2 \, |\boldsymbol{u}_p| \, dA}{\int |\boldsymbol{u}_p|^2 \, |\boldsymbol{u}_p| \, dA}} \quad , \tag{5}$$

where $\boldsymbol{u}_p$ and $\boldsymbol{u}_s$ are the primary and secondary velocity vectors, and dA is an elemental area in the plane of interest. When there is no secondary motion in the plane, $RSKE = 0$, and when the secondary velocity is of comparable magnitude with the primary velocity on an average, $RSKE$ is $O(1)$. The values of $RSKE$ evaluated from the present computations are tabulated in Table 2 for all the planes at the four phase angles considered. In the aortic arch, the values of $RSKE$ increased from planes A to C, except in the decelerating phase where $RSKE$ is highest in plane B. It can be seen from Table 2 that high values of $RSKE$ are found at the entrance region of the branches due to sudden decrease in cross-sectional area. In general, high values of $RSKE$ are noted in the RSCA (planes D, E and F) for all the four phase angles. Within the RSCA, the highest values of $RSKE$ are noted in plane E.

Table 2. Relative secondary kinetic energy ($RSKE$) at several planes at four phase angles.

Plane	$\phi = 0^{\circ}$	$\phi = 75^{\circ}$	$\phi = 130^{\circ}$	$\phi = 320^{\circ}$
A	0.171	0.160	0.297	0.196
B	0.124	0.259	0.584	0.100
C	0.495	0.477	0.432	0.474
D	0.752	0.664	0.926	0.777
E	0.996	1.034	1.060	1.010

F	0.661	0.735	0.514	0.628
G	0.671	0.395	1.202	0.761
H	0.337	0.481	0.339	0.293
I	0.187	0.481	0.257	0.176
J	0.364	0.355	0.353	0.369
K	0.181	0.192	0.168	0.184
L	0.437	0.493	0.349	0.422
M	0.236	0.263	0.271	0.240
N	0.411	0.382	0.478	0.419
O	0.783	1.069	0.644	0.658

3.3. Wall shear stress

In Figure 9 the contours of wall shear stress are plotted in terms of skin friction coefficient, C_f, which is defined as

$$C_f = \frac{\tau_w}{1/2\,\rho\, u_{\max}^2} \quad , \tag{6}$$

where τ_w is the magnitude of the resultant wall shear stress due to all three components of the velocity vector. In general, high C_f values are observed at distal of LSCA and RSCA, the bifurcation of brachiocephalic artery between RSCA and RCA and proximal inner wall of descending aorta during the cardiac cycle. However, the magnitudes of the maximum C_f are different at each phase as can be seen in Figure 9. It is also noted that at the above-mentioned sites C_f is oscillatory, a factor often correlated with atherosclerosis.

In a comprehensive study involving records of 13,827 subjects in a particular hospital the predominant anatomic sites of atherosclerotic occlusive disease were categorized [30]. One of these categories, Category II in their classification, was the bifurcation of the major branches of the aortic arch. Due to this observation and also motivated by the study of [5], the time trace of C_f at select locations in the bifurcation of the aortic branches is monitored. These points and the variation of C_f during the cardiac cycle are shown in Figure 10. The C_f variation is reminiscent of the inlet velocity waveform in Figure 5, with the maximum values of C_f, however, being advanced by up to 5°. This observation is in qualitative agreement with the findings of [5]. The maximum C_f occurs for point 1 which is the brachiocephalic artery bifurcating to RSCA and RCA. Lower values of C_f occur at points 3, 4 and 5. Point 2 had the lowest C_f during the entire cycle. It is important to note that the oscillatory nature of the shear stress and the stress reversal in particular is known to cause fatigue-type of injury to the endothelial cells.

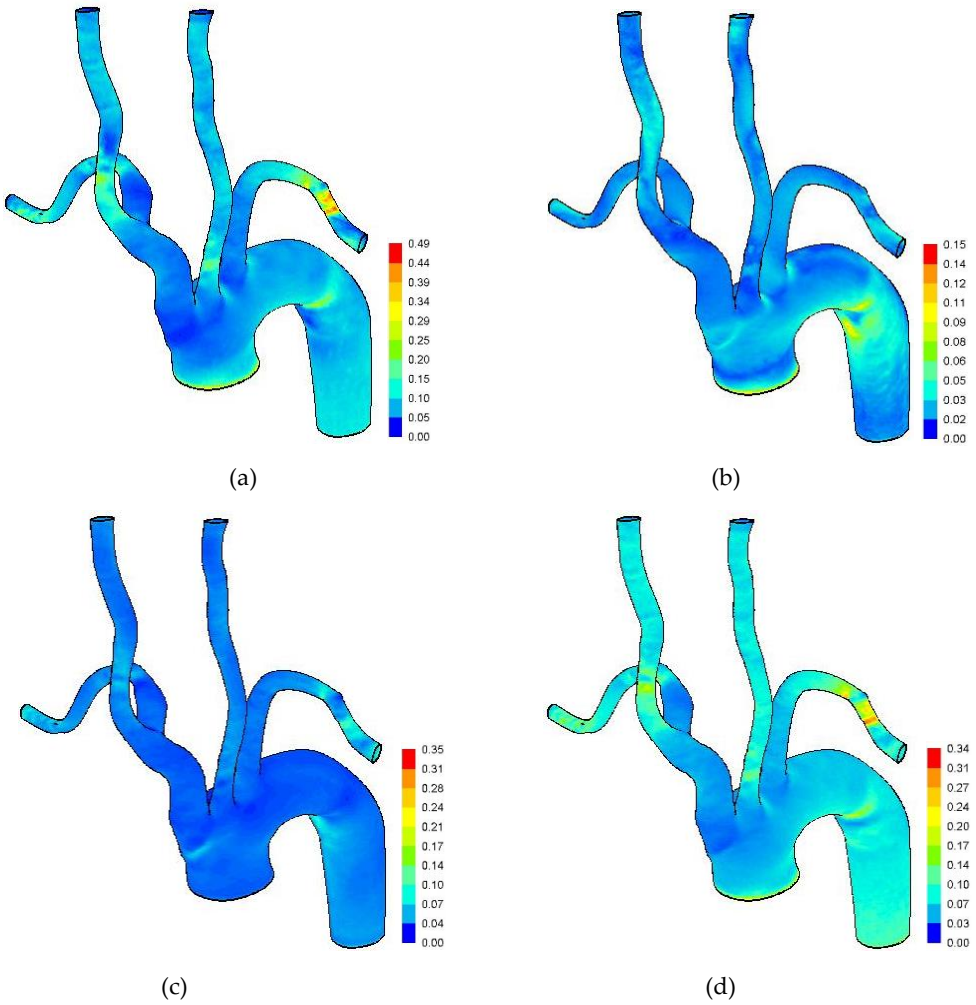

Figure 9. Contours of skin friction coefficient, C_f, at (a) $\phi = 0^\circ$ (b) $\phi = 75^\circ$ (c) $\phi = 130^\circ$ and (d) $\phi = 320^\circ$.

3.4. Streamline patterns

The instantaneous limiting streamlines on the arterial walls are considered next. The limiting streamlines have been one of the most useful constructs in fluid dynamics and this knowledge is applied to study the streamline patterns on the aorta. Several interesting and insightful details are garnered from these patterns.

The streamline patterns on the aorta are shown in Figure 11 for the four phase angles. At $\phi = 0^\circ$, a nodal point of separation (N_s), and below this a saddle point (S_p), are observed at the proximal of descending aorta. Further, two saddle points and a nodal point of separation are found close to each other in the inner wall of the mid-arch. There is a strip of separated region at the beginning of the brachiocephalic artery. In addition to these critical points on the aortic arch, a nodal point of separation is also seen at the distal of LSCA. At $\phi = 75^\circ$, the nodal point of separation and the saddle point at the proximal of descending aorta observed during $\phi = 0^\circ$ came close to each other during this phase. A further interesting observation is the presence of a separated region in the ascending aorta terminating in a separation line (L_s). Two nodes of attachment (N_a) are observed at the entry of the LCA bifurcation. A nodal point of separation is also observed at the bifurcation of brachiocephalic artery towards the RCA. At $\phi = 130^\circ$, there is a nodal point of separation at the proximal of descending aorta, and saddle point and nodal point of attachment are seen at dorsal side of the proximal descending aorta. At $\phi = 320^\circ$, in a remarkable manner, all the flow structures seen in the previous phases vanish due to the

stabilizing nature of the accelerating flow. The application of limiting streamlines to aortic flows helps in identifying the critical points on the aorta wall which is otherwise impossible. Further, using the limiting streamlines, it is observed that all these critical points vanish during the accelerating phase of the cardiac cycle.

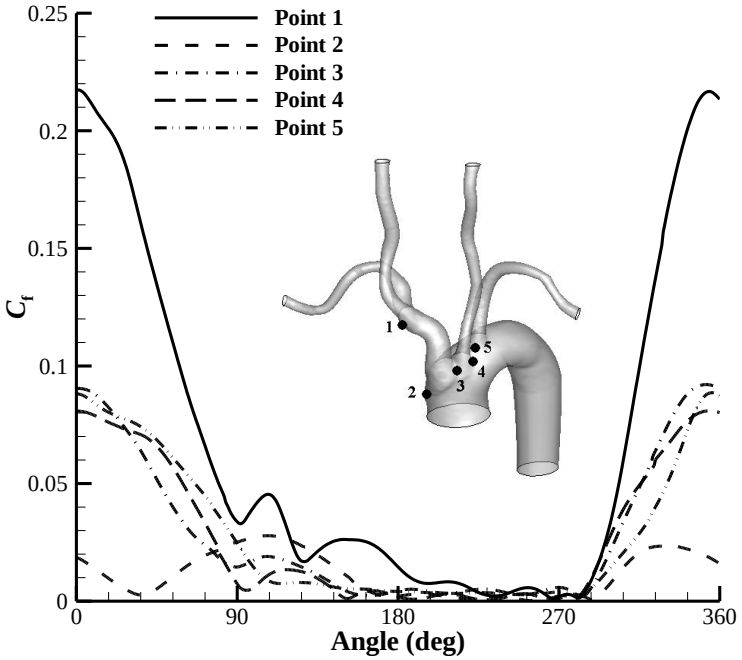

Figure 10. C_f history for five points on the aorta wall.

Several past investigations have hypothesized that hemodynamics plays a major role in atherogenesis. High wall shear regions as the likely areas of localization of atherosclerosis was suggested in [31], while low wall shear stress sites was proposed in [32]. Of course, some of these early findings were motivated by the Reynolds analogy that regions of high shear are usually accompanied by regions of high mass transfer since they are governed by similar transport processes and equations. Later studies elucidated that locations of low mean and oscillating shear stress are the likely predilection locations of atherosclerosis [33]. The wall shear stress plays an important role in the initiation and progression of atherosclerosis [34-36]. The spatial and temporal variation of wall shear stress, along with flow separation and secondary flow, have significant impact on living tissues. This is supported by the fact that the arterial wall remodeling has correlations with low and oscillatory wall shear stress [37]. Further, it has also been postulated that atherosclerotic lesions occur predominantly in regions of low and oscillatory shear stress [38, 39]. In the present study such sites are observed at locations 2, 3, 4, and 5 (i.e. the bifurcation of RCA, LCA and LSCA from the aortic arch) in Figure 10. These regions could possibly be the likely predilection sites for atherosclerosis. This fact is further reinforced by the appearance of a striation of separated flow seen at the bifurcation of RCA from the ascending aorta in Figure 11(a). The application of limiting streamlines to clearly elucidate the complex on-wall flow structures is one of the key contributions of the present study. The limiting streamlines are useful in identifying the flow characteristics which are in turn helpful in pathogenesis before morbidity.

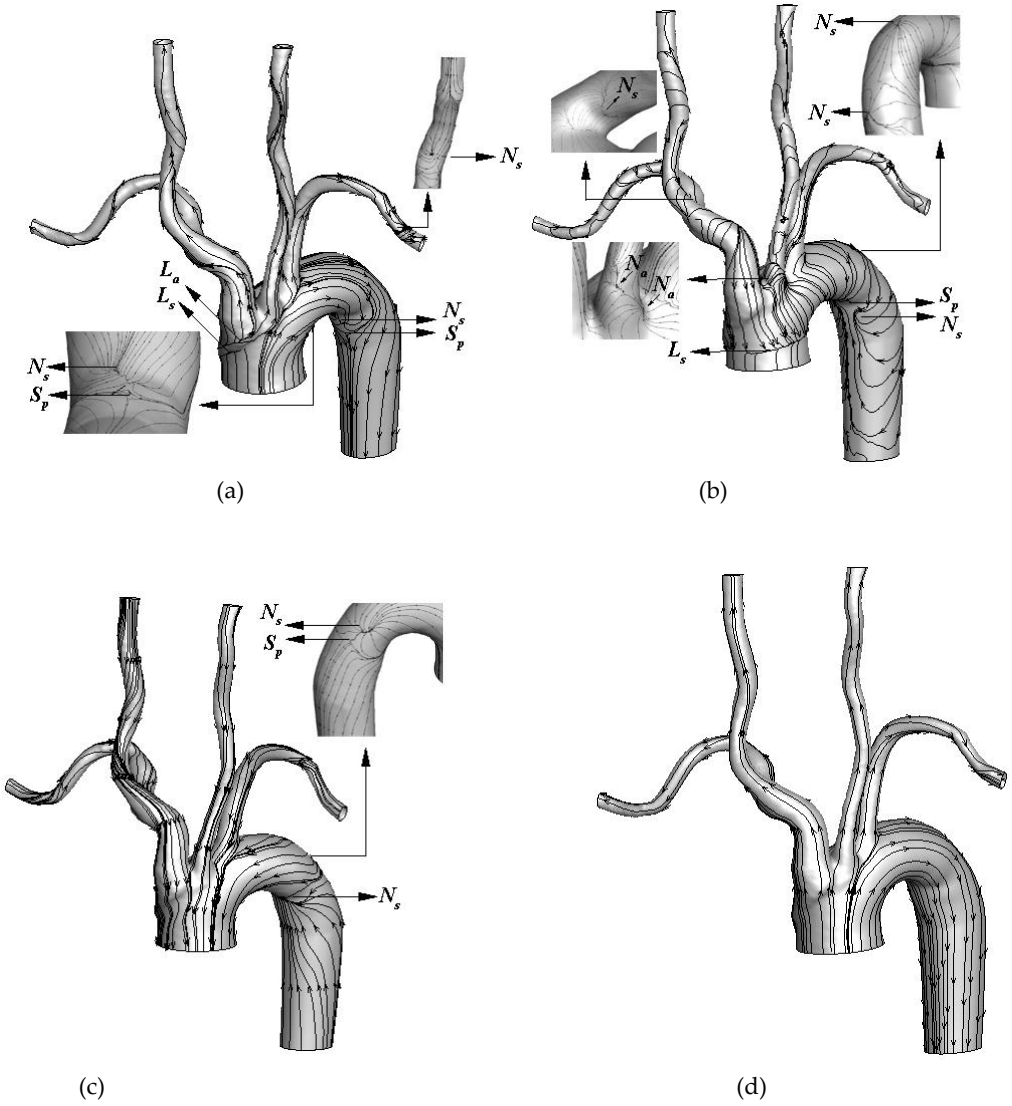

Figure 11. Limiting streamlines at (a) $\phi = 0^{\circ}$ (b) $\phi = 75^{\circ}$ (c) $\phi = 130^{\circ}$ and (d) $\phi = 320^{\circ}$.

The arterial lumen lined with endothelial cells are subjected to spatio-temporal variations in wall shear stress due to the pulsatile nature of the flow. In particular, endothelial cells respond to variations in the magnitude and direction of shear [40, 41]. The endothelial cells being in direct contact with blood detect and communicate changes in blood flow dynamics to the arterial wall and thus act as mechano-signal transducers [41, 42]. Many recent studies have linked low mean and oscillating shear stress as well as stress gradients to the development of early atherosclerotic lesions. The precise biological basis of these findings is still a subject matter of study. However, modifications of endothelial cell structure and function due to variations in wall shear stress are generally thought to be involved. An enhanced understanding of the localization and progression of atherosclerosis can be obtained by studying the endothelial response to blood flow dynamics.

Computational fluid dynamic simulations are gaining importance in understanding disease dynamics, in creating tools for disease management, and finally in designing medical devices. The hemodynamic parameters of interest can be evaluated using subject-specific computational models of complex geometries and this capability has the potential

to improve clinical decision-making. It must be emphasized that further studies are required for enhanced understanding of hemodynamics in the aorta to enable a more precise correlation between the oscillating wall shear stress and atherosclerosis. The present study must be regarded as a step towards that direction.

Moreover, the present study is of value in the context of application of deep learning algorithms in the domain of biomedical engineering. The deep learning algorithms need large amount of data which cannot be obtained from clinical measurements alone. There is a need to create an approach to generate synthetic data mimicking the real data. For instance, 4DFlowNet [43] uses synthetic data to build machine learning models. The machine learning model generates high resolution data points that are useful for clinical purposes. The data from the present study can form the basis for generating huge amount of synthetic data so that machine learning models may be built even when enough clinical datasets are either not available or small.

4. Conclusions

In the present work pulsatile blood flow computations are performed for the three-dimensional aortic arch geometry reconstructed from the CT-scan images of a subject with a physiologically representative pulsatile velocity waveform applied as boundary condition at the inlet of the aorta. It is shown that the blood flow dynamics and wall shear stress patterns are highly subject-specific and the need for accounting actual aortic geometries and boundary conditions for the numerical simulations is emphasized. The contributing aspect of the present study is the observation of complex and asymmetrical flow patterns which are not commonly seen in simple curved pipes or in idealized models of the aortic arch. The primary velocity profiles are skewed towards the inner wall of the aortic arch during the entire cardiac cycle. The flow is seen to be separated at the inner wall of the aorta during the decelerating and reverse flow phases of the cardiac cycle, while it remained attached during the accelerating phase. The secondary flow motion exhibits rich and complex structures. The wall shear stress at the bifurcations of the branches are low and oscillatory and correlates with the preferential sites for atherosclerosis. The flow patterns on the aorta wall are elucidated by plotting the limiting streamlines which show the complex dynamics visually. To the knowledge of the authors', the application of limiting streamlines to aortic flows has not been done previously. Further studies should incorporate more physiologically accurate boundary conditions at the aorta inlet and the outlets obtained from in-vivo measurements to investigate the complex flow patterns observed in this computational study. Such subject-specific flow quantification will be of value to medical practitioners in diagnosis, surgical planning and risk assessment.

Patents: None.

Supplementary Materials: None.

Author Contributions: Conceptualization, Z.S., M.S., V.M.D.P. and R.H.; radiology, V.M.D.P.; image processing, Z.S. and R.H.; computations, Z.S. and M.S.; manuscript preparation, Z.S., M.S., V.M.D.P. and R.H. All authors have read and agreed to the published version of the manuscript.

Funding: This research received no external funding.

Data Availability Statement: All data generated during this study are included in this article itself.

Conflicts of Interest: The authors declare no conflict of interest.

References

[1] Information on http://www.who.int/news-room/fact-sheets/detail/cardiovascular-diseases-(cvds)

[2] A.J. Lusis, Atherosclerosis, Nature 407 (2000) 233-247.
[3] R.M. Nerem, Vascular fluid mechanics, the arterial wall, and atherosclerosis, J. Biomech. Eng. 114 (1992) 274–282.
[4] P.F. Davies, Hemodynamic shear stress and the endothelium in cardiovascular pathophysiology, Nat. Clin. Pract. Cardiovasc. Med. 6 (2009) 16-26.
[5] N. Shahcheraghi, H.A. Dwyer, A.Y. Cheer, A.I. Barakat and T Rutaganira, Unsteady and three-dimensional simulation of blood flow in the human aortic arch, J. Biomech. Eng. 124 (2002) 378-387.
[6] L. Morris, P. Delassus, A. Callanan, M. Walsh, F. Wallis, P. Grace and T. McGloughlin, 3-D numerical simulation of blood flow through models of the human aorta, J. Biomech. Eng. 127 (2005) 767–775.
[7] A.C. Benim, A. Nahavandi, A. Assmann, D. Schubert, P. Feindt and S.H. Suh, Simulation of blood flow in human aorta with emphasis on outlet boundary conditions, Appl. Math. Model. 35 (2011) 3175-3188.
[8] Y. Xuan, Y. Chang, B. Gao and K. Gu, Effect of continuous arterial blood flow of intra-aorta pump on the aorta – a computational study, Appl. Mech. Mater. 275-277 (2013) 672-676.
[9] F. Wang, L. Zhang, L. Wang, C. Li, P. Ge, M. Lian and X. Li, Finite element analysis for the design of branched artificial blood vessel of aortic arch, Appl. Mech. Mater. 302 (2013) 550-555.
[10] C.V. Krishna, N. Gundiah and J.H. Arakeri, Separations and secondary structures due to unsteady flow in a curved pipe, J. Fluid Mech. 815 (2017) 26-59.
[11] C. Zhu, J-H Seo and R. Mittal, Computational modelling and analysis of haemodynamics in a simple model of aortic stenosis, J. Fluid Mech. 851 (2018) 23-49.
[12] M.R. Najjari, C. Cox and M.W. Plesniak, Formation and interaction of multiple secondary flow vortical structures in a curved pipe: transient and oscillatory flows, J. Fluid Mech. 876 (2019) 481-526.
[13] S. Endo, H.L. Goldsmith and T. Karino, Flow patterns and preferred sites of atherosclerotic lesions in the human aorta–I. Aortic arch, Biorheology 51 (2014) 239-255.
[14] S. Numata, K. Itatani, K. Kanda, K. Doi, S. Yamazaki, K. Morimoto, K. Manabe, K. Ikemoto and H. Yaku, Blood flow analysis of the aortic arch using computational fluid dynamics. Eur. J. Cardiothorac. Surg. 49 (2016) 1578-1585.
[15] E. Soudah, J. Casacuberta, P.J. Gamez-Montero, J.S. Perez, M. Rodriguez-Cancio, G. Raush, C.H. Li, F. Carreras and R. Castilla, Estimation of wall shear stress using 4D flow cardiovascular MRI and computational fluid dynamics, J. Mech. Med. Biol. 17 (2017) 1750046.
[16] A.H. Belaghit, B. Aour, M. Larabi and S. Mebarki, Numerical modeling of blood flow in a healthy aorta and aorta with stent, J. Biomimetics, Biomater. Biomed. Eng. 39 (2018) 13-23.
[17] D. Bhuyan, P.R. Babu and J.P. Kalita, Numerical investigation of blood flow characteristics through cannulated aorta, J. Biomimetics, Biomater. Biomed. Eng. 43 (2019) 28-38.
[18] K.B. Chandran, Flow dynamics in the human aorta, J. Biomech. Eng. 115 (1993) 611-616.
[19] J.J.-J, Li, The Arterial Circulation: Physical Principles and Clinical Applications, Springer, New York, 2000.
[20] C.A. Taylor, T.A. Fonte and J.K. Min, Computational fluid dynamics applied to cardiac computed tomography for noninvasive quantification of fractional flow reserve, J. Am. Coll. Cardiol. 61 (2013) 2233-2241.
[21] R.S. Driessen, I. Danad, W.J. Stuijfzand, P.G. Raijmakers, S.P. Schumacher, P.A. van Diemen, J.A. Leipsic, J. Knuuti, S.R. Underwood, P.M. van de Ven, A.C. van Rossum, C.A. Taylor and P. Knaapen, Comparison of computed tomography angiography, fractional flow reserve, and perfusion imaging for ischemia diagnosis, J. Am. Coll. Cardiol. 73 (2019) 161-173.
[22] CT-Flow, The modern way to diagnose coronory artery disease, HeartFlow, Inc. 2019.
[23] A. Coenen, M.M. Lubbers, A. Kurata, A. Kono, A. Dedic, R.G. Chelu, M.L. Dijkshoorn, F.J. Gijsen, M. Ouhlous, R-J.M. van Genus and K. Nieman, Fractional flow reserve computed from noninvasive CT angiography data: diagnostic performance of an on-site clinician-operated Computational fluid dynamics algorithm, Radiology 274 (2015) 674-683.
[24] W. Jiang, Y. Pan, Y. Hu, X. Leng, J. Jiang, L. Feng, Y. Xia, Y. Sun J. Wang, J. Xiang and C. Li, Diagnostic accuracy of coronory computed tomography angiography-derived fractional flow reserve, BioMed. Eng. Online 20 (2021) 1-12.
[25] M.D. Deshpande, V. Ballal, S.R. Shankapal, V.M.D. Prabhu and M.G. Srinath, Subject-specific blood flow simulation in the human carotid artery bifurcation, Curr. Sci. 97 (2009) 1303-1312.
[26] I.B. Celik, U. Ghia, P.J. Roache, C.J. Freitas, H. Coleman and P.E. Raad, Procedure for estimation of uncertainty due to discretization in CFD applications, J. Fluids Eng. 130 (2008) 078001.
[27] Y. Agrawal, L. Talbot and K. Gong, Laser anemometer study of flow development in curved circular pipes, J. Fluid. Mech. 85 (1978) 497-518.
[28] K.E. Barrett, S.M. Barman, S. Boitano and H. Brooks, Ganong's Review of Medical Physiology, 23rd ed., McGraw-Hill Medical, New York, 2009.
[29] A. Guha and K. Pradhan, Secondary motion in three-dimensional branching networks. Phy. Fluids, 29 (2017) 063602.
[30] M.E. DeBakey, G.M. Lawrie and D.H. Glaeser, Patterns of atherosclerosis and their surgical significance. Ann. Surg. 201 (1985) 115-131.
[31] D.L. Fry, Responses of the arterial wall to certain physical factors, in: R. Porter, J. Knight (Eds.), Ciba Foundation Symposium 12 - Atherogenesis: Initiating Factors, Elsevier, Amsterdam, 1973.
[32] C.G. Caro, J.M. Fitz-Gerald and R.C. Schroter, Atheroma and arterial wall shear: observation, correlation and proposal of a shear dependent mass transfer mechanism for atherogenesis, Proc. R. Soc. Lond B Biol. Sci. 177 (1971) 109-159.

[33] D.N. Ku, D.P. Giddens, C.K. Zarins and S. Glagov, Pulsatile flow and atherosclerosis in the human carotid bifurcation: Positive correlation between plaque location and low oscillating shear stress, Arteriosclerosis 5 (1985) 293-302.
[34] A.M. Shaaban and A.J. Duerinckx, Wall shear stress and early atherosclerosis: a review, AJR Am. J. Roentgenol. 174 (2000) 1657-1665.
[35] C. Cheng, R. de Crom, R. van Haperen, F. Helderman, B.M. Gourabi, L.C.A. van Damme, S.W. Kirschbaum, C.J. Slager, A.F.W. van der Steen and R. Krams, The role of shear stress in atherosclerosis: action through gene expression and inflammation? Cell Biochem. Biophys. 41 (2004) 279-294.
[36] K.S. Cunningham and A.I. Gotlieb, The role of shear stress in the pathogenesis of atherosclerosis, Lab. Investig. 85 (2005) 9-23.
[37] C.R. White and J.A. Frangos, The shear stress of it all: the cell membrane and mechanochemical transduction, Philos. Trans. R. Soc. B. 362 (2007) 1459-1467.
[38] E. Cecchi, C. Giglioli, S. Valente, C. Lazzeri, G.F. Gensini, R. Abbate and L. Mannini, Role of hemodynamic shear stress in cardiovascular disease, Atherosclerosis 214 (2011) 249-256.
[39] J. Moore, C. Xu, S. Glagov, C.K. Zarins and D.N. Ku, Fluid wall shear stress measurements in a model of the human abdominal aorta: oscillatory behavior and relationship to atherosclerosis, Atherosclerosis 110 (1994) 225-240.
[40] D.P. Giddens, C.K. Zarins and S. Glagov, The role of fluid mechanics in the localisation and detection of atherosclerosis, J. Biomech. Eng. 115 (1993) 588-594.
[41] S.G. Frangos, V. Gahtan and B. Sumpio, Localisation of atherosclerosis: role of hemodynamics, Arch. Surg. 134 (1999) 1142-1148.
[42] K.B. Chandran, A.P. Yoganathan and S.E. Rittgers, Biofluid Mechanics-The Human Circulation, CRC Press, New York, 2007.
[43] Ferdian, A. Suinesiaputra, D.J. Dubowitz, D. Zhao, A. Wang, B. Cowan and A.A. Young, 4DFlowNet: super-resolution 4D flow MRI using deep learning and computational fluid dynamics, Front. Phys. 8 (2020) 1-14.